Project Acronym	CORMORAN (ANR 11-INFR-010)
Document Title	D2.1b - On-Body Antennas Characterization & Exploitable Radiation Properties – **Updated Document : 3D Deterministic Modeling of Electromagnetic Wave Interactions with a Dielectric Cylinder**
Contractual Date of Delivery	M10 (31/10/2012)
Actual Date of Delivery	M10 (31/10/2012)
Editor	UR1
Authors	Eric PLOUHINEC
Participants	UR1
Related Task(s)	T2
Related Sub-Task(s)	T2.1
Security	Public
Nature	Technical Appendix
Version Number	1.0
Total Number of Pages	27

TABLE OF CONTENT

ABSTRACT

This D2.1 updated document describes an additional work realized for the On-Body antennas characterization in the CORMORAN project: the deterministic modeling of electromagnetic wave interactions with a dielectric cylinder. A first additive 3D model has already been presented in section 5.2 of [Mhedhbi 1] taking into account the presence of a dielectric cylinder in the immediate proximity of an electromagnetic source, derived from [McNamara]. But this model only considers the reflection of the electromagnetic wave with the dielectric cylinder using Geometrical Optics (GO). Moreover, direct and reflected rays are considered to arrive in the same direction at the observation point, i.e. the observation point is considered to be far from the cylinder. Therefore, the phenomenon of "creeping" waves was not considered and there was a problem when the source and the observation points were in Non Line Of Sight (NLOS) configuration, i.e. when the observation point was in the shadow region, because this first model predicted no received field in this configuration. Moreover, the observation point position was not taken into account. So the idea was to develop a 3D model able to take into account, not only the reflected wave but also the 2 diffracted (or "creeping") waves existing in the shadow region as well as in the lit region. This prediction model is based on the well-known Uniform Theory of Diffraction (UTD) for the modeling of the electromagnetic waves interactions and the ray-tracing technique for the electromagnetic wave paths search. In this updated document of [Mhedhbi 1], this model is described in details with its major UTD formulations. Then it is validated in 2D with a conducting and a dielectric cylinder using reference literature articles [McNamara][Pathak][Hussar]. Concerning the 3D approach, it has been validated with the measurement of [Govaerts] for a conducting cylinder. Finally it has been compared with the measurement Series S2 of [Mhedhbi 1], in the 2D configuration, giving results very close to the measurements.

EXECUTIVE SUMMARY

This document presents the additional studies made on the deterministic modeling of an electromagnetic wave propagation, in presence of a 3D dielectric cylinder. This model implies 2 steps: first, the search of the electromagnetic wave paths in the lit (Line Of Sight (LOS) case) and in the shadow (Non Line of Sight (NLOS) case) regions, using a ray-tracing technique and, secondly, the received field computation using the Uniform Theory of Diffraction (UTD). The principal novelties, in comparison with the 3D additive model described in [Mhedhbi 1], are the modeling of the diffracted or "creeping" waves on the cylinder and the observation point position consideration. First, the ray-tracing technique is described explaining how we find the reflected and diffracted paths of the electromagnetic wave in 2D as well as in 3D configurations. Secondly, the UTD principal formulations, allowing the computation of the total electromagnetic field at the observation point, are presented. Then, the model is validated in 2D with a conducting [McNamara][Pathak] and a dielectric [Hussar] cylinder. It is also validated in 3D with a conducting cylinder [Govaerts]. This model also gives results very close to the measurement series S2 of [Mhedhbi 1] in the 2D configuration.

1. INTRODUCTION

This Document is related to the subtask 2.1 of the CORMORAN project and is an Appendix of the Technical Report [Mhedhbi 1]. This subtask focused on investigating and modeling the interaction of the antenna with the body, according to its orientation and proximity.

In this project, the UR1 team is particularly in charge of the WBAN channel modelling. One possibility is then the deterministic WBAN channel modelling using UTD (Uniform Theory of Diffraction). UTD allows the received electromagnetic field computation associated with ray-tracing. This theory is only used with canonical shapes implying that human body could be modelled by cylinders, which is one of the solutions explored by the CORMORAN Project for the Channel Modelling. The cylinder could model, for instance, an arm, the trunk or a leg.

In this updated document, a deterministic 3D propagation prediction model is presented, specific to the electromagnetic wave propagation in the presence of a 3D circular dielectric cylinder. The used ray-tracing technique and the UTD formulations are detailed. Then, this model has been validated in 2D with a conducting [McNamara][Pathak] and a dielectric cylinder [Hussar], and in 3D with a conducting cylinder [Govaerts]. This model is also particularly compared to the measurement series S2 of the characterization of body-worn antennas relying on a specific over-the-air (OTA) test-bed in anechoic chamber and a near-field antenna measurement chamber [Mhedhbi 1].

This document is structured as follows: in Section 2, we describe the specific 3D ray-tracing used for an electromagnetic source in presence of a circular dielectric cylinder. Then, in Section 3, the specific UTD formulations, used for the computation of the total received electromagnetic field, are given. In Section 4, we focus on the validation of the used theoretical formulations of the model with articles of the literature in 2D (conducting and dielectric cases) and in 3D (conducting case). Finally, in Section 5, we make a comparison of this UTD model with measurement series S2 of [Mhedhbi 1] in a 2D configuration.

In this technical Appendix, the UTD deterministic channel modelling is only described for the "Scattering" case, i.e. Transmitter and Receiver far from the cylinder. Two other cases could be modelled with UTD:

- "Radiation" case when the Transmitter (the Receiver) is on the cylinder and the Receiver (the Transmitter) is far from the cylinder.
- "Coupling" case when both Transmitter and Receiver are on the cylinder.

These two last cases are not described in this Appendix but will be studied later.

2. 3D RAY-TRACING

Before applying UTD, we have to find the different paths followed by the electromagnetic wave. For this first step, we use the ray-tracing technique: we can model electromagnetic waves paths by rays because the used frequencies for WBAN propagation are sufficiently high. The basic canonical shape is the cylinder because this canonical shape seems to be the best shape to model the different parts of the human body.

In this document, we focus on the electromagnetic wave interactions with only one circular cylinder. To perform the ray-tracing, we have to look for the different rays existing between a Transmitter Tx and a Receiver Point P in presence of a 3D finite length cylinder. Two scenarios can exist:

- Tx and P could be in Line Of Sight (LOS): then P is in the <u>L</u>it region (it will be called P_L in this document);
- Tx and P could be in Non Line Of Sight (NLOS): then P is in the <u>S</u>hadow region (it will be called P_S in this document).

Depending on the observed scenario, the rays nature won't be the same, as will be explained in the following paragraphs.

Moreover, the cylinder axis is not necessarily the z axis: it could be anywhere in the Cartesian coordinates system. Concerning Tx and P positions, they also could be placed anywhere but not too close to the cylinder because, for the moment, we only study the UTD "Scattering" case.

2.1. LOS CASE

In the LOS configuration, we find necessarily 4 rays, as illustrated by Figure 2-1:

- 1 direct ray (in yellow),
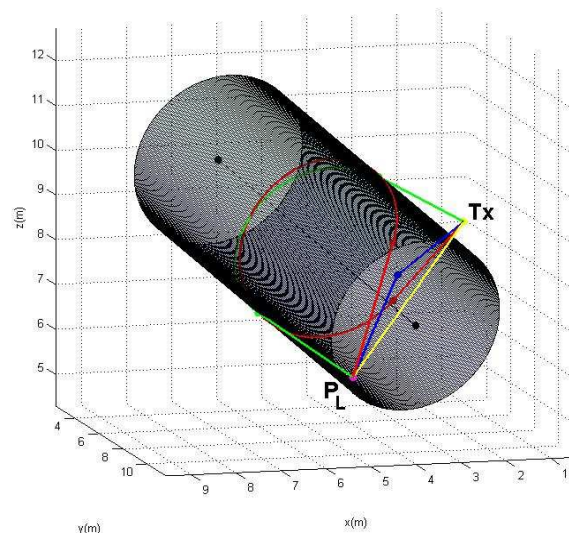- 1 reflected ray (in blue),
- 2 diffracted rays (in red and green).

Figure 2-1: 3D ray-tracing example for a LOS case

First, the problem of finding the reflection point Q_R in 2D could not be solved by ruler and compass. The reflection point in the 2D configuration could be obtained using:

i) a quartic equation [Glaeser] but only one solution of this equation is geometrically valid. Unfortunately, "forbidden regions" and numerical instabilities imply additional tests that can slow down the solution getting.

ii) the minimization of the scalar product "$\vec{n} \cdot \left(\overrightarrow{TxQ_R} + \overrightarrow{Q_R P_L} \right)$" where $\vec{n}$ is the circle normal at Q_R. An optimization function is then necessary to obtain the solution.

The second solution was finally adopted: it is slightly faster and doesn't need additional tests. Then, to obtain the reflection point in the 3D configuration, we have found a plane where Thales theorem could be used, giving us the height of the reflection point (abscissa and ordinate were already obtained using the 2D configuration).

Secondly, to find the diffracted rays, we have to find the attachment and the detachment points of the "creeping" part of the diffracted rays on the cylinder. They are easily obtained in the 2D configuration using trigonometric formulas [McNamara]. To obtain the heights of these attachment and detachment points (i.e. the 3D configuration), we have to notice that the "creeping" part of the ray is necessarily a geodesic of the cylinder. If we "unfold" the cylinder, it becomes a plane and this geodesic becomes a straight line: then, using the Thales theorem in the appropriated planes, we easily find the heights of the attachment and detachment points.

Finally, we could notice that the length of the cylinder is finite : so tests are needed to verify that reflection, attachment or detachment points belong to the cylinder.

2.2. NLOS CASE

A 3D ray-tracing example is given by Figure 2-2 for the NLOS configuration: only 2 diffracted rays are present (in red and green).
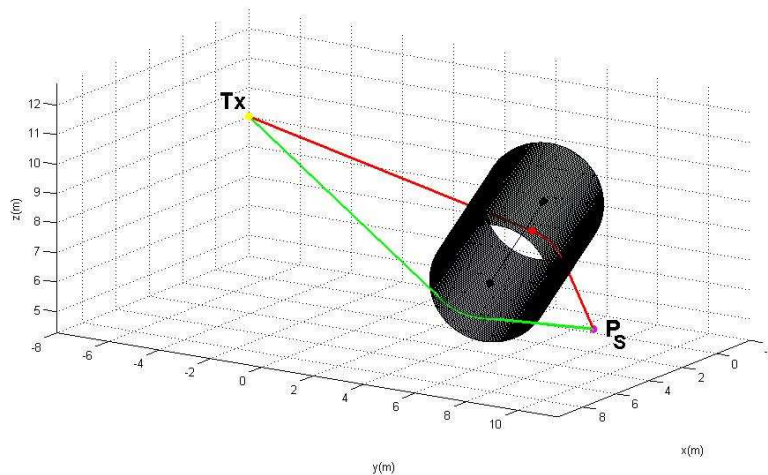

Figure 2-2: 3D ray-tracing example for a NLOS case

The technique for finding the attachment and detachment points of these rays is, of course, the same as the one described in the previous paragraph for the LOS case.

3. INTERACTIONS MODELING WITH UNIFORM THEORY OF DIFFRACTION

Knowing the different paths taken by the electromagnetic wave thanks to the ray-tracing step, we can compute the 3D total received electromagnetic field, for the 2 polarizations, using UTD.

3.1. GEOMETRICAL OPTICS FORMALISM

The UTD received field computation uses the same formalism as the well-known Geometrical Optics (GO). So, in a general case, the UTD received field E^R, after one interaction, could be expressed versus the incident field E^i as:

$$\begin{bmatrix} E_{//}^R(s^R) \\ E_{\perp}^R(s^R) \end{bmatrix}_{B^R} = \sqrt{\frac{\rho_1}{\rho_1 + s^R} \cdot \frac{\rho_2}{\rho_2 + s^R}} \begin{bmatrix} Inter_{//} & 0 \\ 0 & Inter_{\perp} \end{bmatrix} \begin{bmatrix} E_{//}^i(s^i) \\ E_{\perp}^i(s^i) \end{bmatrix}_{B^i} \cdot e^{-jks^R} \qquad (1)$$

where:
- k is the wave number;
- s^R is the distance between the interaction point and the Receiver Point;
- s^i is the distance between the Transmitter and the Interaction Point;
- B^i and B^R are local bases associated with the ray before the interaction and the ray after the interaction respectively;
- $Inter_{//}$ and $Inter_{\perp}$ are the interaction coefficients for parallel (//) and perpendicular ($\perp$) polarizations respectively;
- ρ_1 and ρ_2 are the radius of curvature of the field after the interaction.

Finally, in equation (1), the term under the square root is called the divergence factor of the field and the matrix containing coefficients $Inter_{//}$ and $Inter_{\perp}$ is called the interaction matrix.

3.2. TOTAL RECEIVED FIELD EXPRESSION

To well understand the possible expressions of the total UTD received field, the interaction points will be represented, in this part, considering the top view of the cylinder. The 2 diffracted rays exist for LOS <u>and</u> NLOS cases. The first diffracted ray (ray 1), represented in red, will be the clockwise ray with an attachment point Q_1 and a detachment point Q_2. The second diffracted ray (ray 2), represented in green, will be the counterclockwise ray with an attachment point Q_3 and a detachment point Q_4.
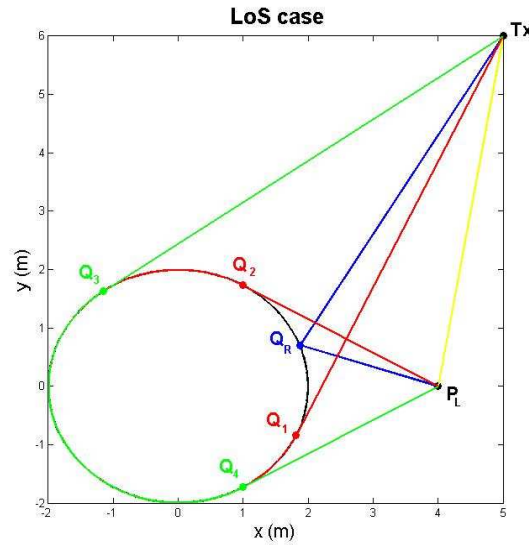
3.2.1 LOS CASE

Figure 3-1: Ray-tracing top view example for a LOS scenario

The Total field $E^T_{//,\perp}$ at the Observation Point P_L is the sum of 3 fields due to the 3 found rays:

$$E^T_{//,\perp}(P_L) = E^i_{//,\perp}(P_L) + E^r_{//,\perp}(P_L) + E^d_{//,\perp}(P_L) \tag{2}$$

where:

- the Incident field $E^i_{//,\perp}$, considering a spherical wave at the Transmitter Tx, is expressed as :

$$E^i_{//,\perp}(P_L) = C_0 \cdot \frac{e^{-jks^0}}{s^0} \tag{3}$$

with s^0 the distance between Tx and P_L, and C_0 a constant associated with the Incident field power.

- the Reflected field $E^r_{//,\perp}$ is expressed as:

$$E^r_{//,\perp}(P_L) = \sqrt{\frac{\rho^r_1 \cdot \rho^r_2}{(\rho^r_1 + s^r) \cdot (\rho^r_2 + s^r)}} . R_{//,\perp} \cdot E^i_{//,\perp}(Q_R) \cdot e^{-jks^r} \tag{4}$$

with Q_R the reflection point (cf. Figure 3-1), s^r the distance between Q_R and P_L, $R_{//,\perp}$ the reflection coefficient depending on polarization, and ρ^r_1 and ρ^r_2 the radius of curvature of the reflected field.

- the total Diffracted field $E^d_{//,\perp}$ is the sum of the 2 diffracted fields and expressed as:

$$E_{//,\perp}^{d}(P_L) = E_{//,\perp}^{d1}(P_L) + E_{//,\perp}^{d2}(P_L) \tag{5}$$

with the diffracted field associated with ray 1 expressed as:

$$E_{//,\perp}^{d1}(P_L) = \sqrt{\frac{\rho_{1,2}^{d}}{s_1^{d} \cdot (\rho_{1,2}^{d} + s_1^{d})}} . T_{//,\perp}^{1} \cdot \sqrt{\frac{d\eta(Q_1)}{d\eta(Q_2)}} E_{//,\perp}^{i}(Q_1) \cdot e^{-jks_1^{d}} \tag{6}$$

and the diffracted field associated with ray 2 expressed as:

$$E_{//,\perp}^{d2}(P_L) = \sqrt{\frac{\rho_{2,2}^{d}}{s_2^{d} \cdot (\rho_{2,2}^{d} + s_2^{d})}} . T_{//,\perp}^{2} \cdot \sqrt{\frac{d\eta(Q_3)}{d\eta(Q_4)}} E_{//,\perp}^{i}(Q_3) \cdot e^{-jks_2^{d}} \tag{7}$$

For these last diffracted fields, we have to describe the following characteristics:

- $T_{//,\perp}^{1}$ $(resp. T_{//,\perp}^{2})$ is the diffraction coefficient depending on polarization, associated with diffracted ray 1 (resp. ray 2).

- s_1^{d} $(resp. s_2^{d})$ is the distance between Q_2 (resp. Q_4) and P_L.

- $\sqrt{\frac{d\eta(Q_1)}{d\eta(Q_2)}}$ $\left(resp. \sqrt{\frac{d\eta(Q_3)}{d\eta(Q_4)}}\right)$ illustrates the conservation of energy flux in the surface-ray strip from Q_1 to Q_2 (resp. from Q_3 to Q_4).

- $\rho_{1,2}^{d}$ $(resp. \rho_{2,2}^{d})$ is the second radius of curvature of the diffracted ray 1 (resp. ray 2).
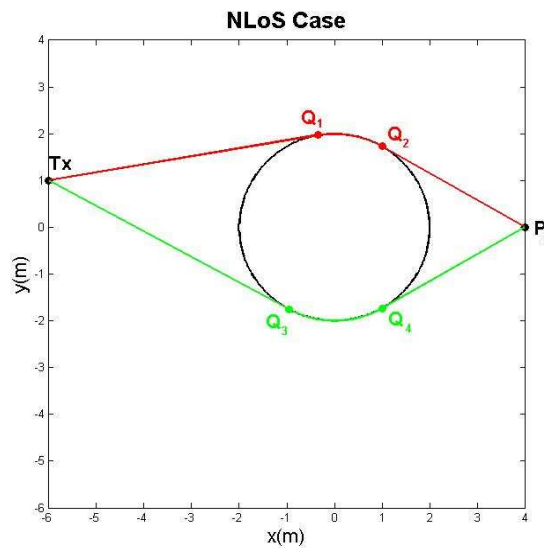
3.2.2 NLOS CASE

Figure 3-2: Ray-tracing top view example for a NLOS scenario

The Total field $E_{//,\perp}^{T}$ at the Receiver Point P_S is only the total diffracted field expressed as:

$$E_{//,\perp}^{T}(P_S) = E_{//,\perp}^{d}(P_S)$$

(8)

with:

$$E_{//,\perp}^{d}(P_S) = E_{//,\perp}^{d1}(P_S) + E_{//,\perp}^{d2}(P_S)$$

(9)

$E_{//,\perp}^{d1}(P_S)$ and $E_{//,\perp}^{d2}(P_S)$ are the diffracted fields at P_S for diffracted ray 1 and ray 2 respectively. They have, of course, the same expressions as the diffracted fields expressed by equations (6) and (7) replacing P_L by P_S, using the Q_i (i=1, 2, 3, 4) points of Figure 3-2.

3.3. INTERACTION COEFFICIENTS

3.3.1 REFLECTION COEFFICIENTS

The Reflection coefficients $R_{//,\perp}$ of equation (4) depend on polarization and are expressed as:

$$R_{//,\perp} = -\sqrt{\frac{-4}{\xi_L}} \cdot e^{-j(\xi_L)^3/12} \cdot \left[\frac{e^{-j\pi/4}}{2\xi_L\sqrt{\pi}} [1 - F(X_L)] + \hat{P}_{//,\perp}(\xi_L) \right]$$

(10)

with:

- the Fock parameter ξ_L associated with the reflected field in the Lit region expressed as:

$$\xi_L = -2m_R \cdot \cos\theta^i$$

(11)

$m_R = \left(\frac{kR_{cR}}{2} \right)^{\frac{1}{3}}$ is the curvature parameter depending on R_{cR}, radius of curvature of

the cylinder at the reflection point Q_R, and θ^i is the angle of reflection.

- the argument of the transition function X_L formulated as:

$$X_L = 2kL_L \cos^2(\theta^i)$$

(12)

for which L_L is a distance parameter expressed as:

$$L_L = \frac{s^r \cdot s_r^i}{s^r + s_r^i}$$

(13)

with s_r^i the distance between the transmitter Tx and the reflection point Q_R.

3.3.2   DIFFRACTION COEFFICIENTS

The Diffraction Coefficients $T_{//,\perp}^1$ and $T_{//,\perp}^2$ of equations (6) and (7), corresponding to diffracted rays 1 and 2, also depend on polarization and are expressed, for a circular cylinder, as:

$$T_{//,\perp}^{1,2} = -m_{1,2} \cdot \sqrt{\frac{2}{k}} \cdot e^{-jkt_{1,2}} \cdot \left[\frac{e^{-j\pi/4}}{2\xi_{d1,2}\sqrt{\pi}} [1 - F(X_{d1,2})] + \hat{P}_{//,\perp}(\xi_{d1,2}) \right] \tag{14}$$

In this equation, $m_{1,2} = \left(\dfrac{kR_{c1,2}}{2} \right)^{\frac{1}{3}}$ is the curvature parameter depending on R$_{c1}$ (resp. R$_{c2}$), radius of curvature of the cylinder at Q$_1$ or Q$_2$ (resp. Q$_3$ or Q$_4$) for ray 1 (resp. ray 2). t$_1$ (resp. t$_2$) is the 3D distance between Q$_1$ and Q$_2$ (resp. Q$_3$ and Q$_4$) on the cylinder: it corresponds to the length of the circular cylinder geodesic (which is necessarily a circular helix) between Q$_1$ and Q$_2$ (resp. Q$_3$ and Q$_4$). We have also 2 additional parameters:

- the Fock parameter $\xi_{d1,2}$, associated with the diffracted ray 1 or 2, expressed as:

$$\xi_{d1,2} = \frac{m_{1,2}}{R_{c1,2}} \cdot t_{1,2} \tag{15}$$

- the argument of the transition function $X_{d1,2}$ expressed as:

$$X_{d1,2} = \frac{kL_{d1,2}(\xi_{d1,2})^2}{2(m_{1,2})^2} \tag{16}$$

depending also on the ray number. $L_{d1,2}$ is a distance parameter defined as:

$$L_{d1,2} = \frac{s_{1,2}^d \cdot s_{1,2}^i}{s_{1,2}^d + s_{1,2}^i} \tag{17}$$

depending on the ray number. $s_1^i \left(resp.\ s_2^i \right)$ is the distance between Q$_1$ (resp. Q$_3$) and Tx.

3.4. SPECIAL FUNCTIONS

In equations (10) and (14), special mathematical functions $F(X)$ and $\hat{P}_{//,\perp}(\xi)$ appeared in the expressions of reflection and diffraction coefficients respectively. They are the heart of the UTD model developed in this document.

3.4.1   TRANSITION FUNCTION

The Transition Function $F(X)$ is a UTD specific function and was used initially for UTD Wedge Diffraction [Kouyoumjian]. It is defined as:

$$F(X) = 2j\sqrt{X}\, e^{jX} \int_{\sqrt{X}}^{\infty} e^{-jt^2}\, dt \tag{18}$$

We have $F(X) \to 1$ when $X \gg 1$ and $F(X) \to 0$ when $X \to 0$.

3.4.2   PEKERIS FUNCTION

The Pekeris function $\hat{P}_{//,\perp}(\xi)$ is a function specifically used for describing mathematically the phenomenon of "creeping" waves (or waves diffracted by a cylinder). Its formulation is the following:

$$\hat{P}_{//,\perp}(\xi) = \frac{e^{-j\frac{\pi}{4}}}{\sqrt{\pi}} \int_{-\infty}^{\infty} e^{-j\xi t} \cdot \frac{V'(t) - q_{//,\perp} \cdot V(t)}{W_2'(t) - q_{//,\perp} \cdot W_2(t)}\, dt \tag{19}$$

"Fock-Airy" functions $V(t)$, $V'(t)$, $W_2(t)$ and $W_2'(t)$ appearing in equation (19) could be expressed according to Airy functions $Ai(t)$, $Ai'(t)$, $Bi(t)$ and $Bi'(t)$ [Plouhinec] as:

$$
\begin{aligned}
V(t) &= \sqrt{\pi} \cdot Ai(t) \\
V'(t) &= \sqrt{\pi} \cdot Ai'(t) \\
W_2(t) &= \sqrt{\pi}\big(Bi(t) - j \cdot Ai(t)\big) \\
W_2'(t) &= \sqrt{\pi}\big(Bi'(t) - j \cdot Ai'(t)\big)
\end{aligned}
\tag{20}
$$

Moreover, among all the equations given before, this function is the only term that takes into account the polarization of the wave and the dielectric nature of the cylinder. Indeed, these 2 important physic parameters take place in the $q_{//,\perp}$ parameter of equation (19), described as:

$$q_{//} = -j\frac{m}{K} \quad and \quad q_{\perp} = -jmK \tag{21}$$

m is the curvature parameter described before, depending on the ray curvature at the considered interaction point, and K takes into account the dielectric nature of the cylinder as:

$$K = \sqrt{\varepsilon_r} = \sqrt{\varepsilon_r' - j\big[\varepsilon_r'' + 60\lambda\sigma\big]} \tag{22}$$

ε_r is the complex permittivity of the cylinder. $\varepsilon_r^{'}$ and $\varepsilon_r^{''}$ are the real and imaginary parts of the relative permittivity of the cylinder respectively. λ is the wavelength and σ is the conductivity of the cylinder. If we use a conducting cylinder, $\sigma \rightarrow +\infty$, $K \rightarrow +\infty$ and, consequently, $q_{//} \rightarrow 0$ and $q_\perp \rightarrow +\infty$.

Airy functions already exist in Matlab software used for developing this 3D propagation model. So, the main difficulty was the computation of the integral appearing in equation (19). For this, 3 different techniques were used to compute the Pekeris functions, depending on the ξ value:

1. for $\xi < -3$: the Stationary Phase method [Bouche];
2. for $-3 \leq \xi \leq 3$: the Filon Technique [Abramovitz][Wait][Pearson][Plouhinec];
3. for $\xi > 3$: a Sum of Residues limited to 10 terms (sufficient for the sum convergence) [Pathak] [Medgyesi][Plouhinec].

4. MODEL VALIDATION

For this section and section 5 of this report, the cylinder is considered to be circular with a radius R. ϕ is the azimuth angle, considered from the x axis. θ is the elevation angle, considered from the z axis. The boundary separating the Lit zone from the Shadow zone is called the SSB (for *Surface Shadow Boundary*).

4.1. 2D VALIDATION WITH LITERATURE ARTICLES

We have first to verify if the proposed propagation model gives the waited results in the 2D configuration for a conducting and a dielectric cylinder. For this first approach, literature articles giving good results seem sufficient to validate our model code.

4.1.1   CONDUCTING CASE

For this validation, we use the results of [McNamara] and [Pathak]: their conducting cylinder scenarios were the same, i.e. the source is considered to be on the x axis with an abscissa equal to 2λ and R=λ. The Receiver Point is considered to be far from the cylinder. Consequently, the SSB corresponds to an azimuth angle ϕ = 150°. Furthermore, the emitted wave is considered spherical.

The first idea was to verify the necessity to take into account the diffracted rays in the Lit region. Figure 4-1 (a) (resp. (b)) gives exactly the same results as Figure 8.12 (resp. Figure 8.13) of [McNamara] for which q = 0. Figure 4-1(a) gives the total received field but with the diffracted field included only in the shadow region (ϕ > 150°): we note a discontinuity at the SSB. Figure 4-1(b) includes the surface-diffracted field in the Lit zone (ϕ < 150°): the total field now is continuous across the SSB. Figure 4-1 emphasizes that, although the UTD solution is known as the shadow zone solution, it also exists in the lit zone if the scattering object is closed.

After this first verification, we have considered the same scenario as before but working with the 2 polarizations and the Receiver point turning around the cylinder, i.e. 0° < ϕ < 360°: this

case was treated in [Pathak]. Figures 4-2(a) and 4-2(b) gives the results for this scenario for ⊥ and // polarizations respectively. They give exactly the same results as the Figures 7(a) and 7(b) of [Pathak] respectively, validating our propagation model for a 2D conducting cylinder.
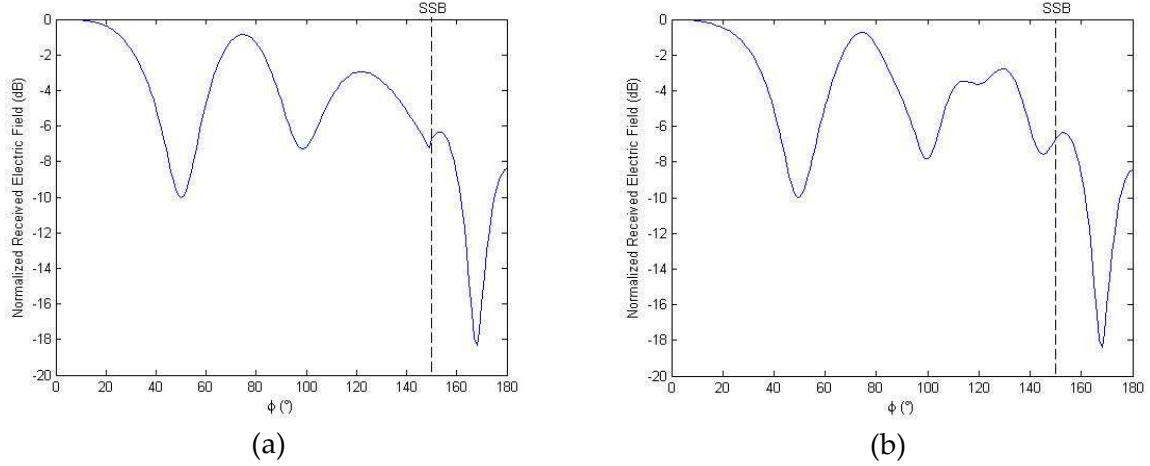

(a)

(b)

Figure 4-1: Results for the scenario of Figures 8-12 and 8.13 of [McNamara]:
- **(a) with the diffracted rays contribution omitted from the Lit zone**
- **(b) with the diffracted rays contribution included in the Lit zone**

(a)

(b)
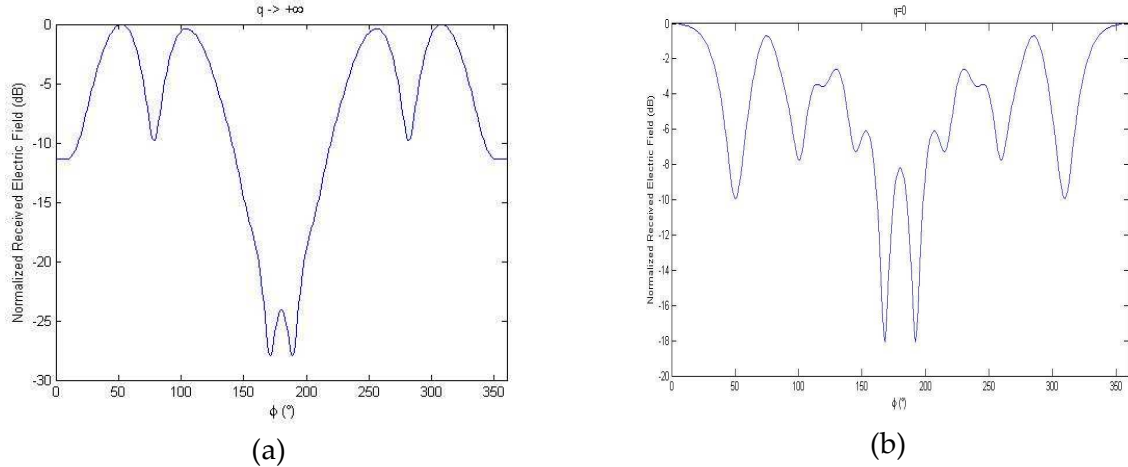
Figure 4-2: Results for the scenario of Figures 7(a) and 7(b) of [Pathak]
for (a) polarization ⊥ and (b) for polarization //

4.1.2 DIELECTRIC CASE

In this case, the validation is obtained from Figure 5 of [Hussar]. The dielectric nature of the cylinder is defined by:

$$q = \left(\frac{kR}{2} \right)^{\frac{1}{3}} \cdot C \tag{23}$$

with *C=0,25.j* and *kR = 20*. Moreover, we have $kr_1 = 25$ with r_1 the abscissa of the line source (i.e. cylindrical emitted wave) and *kr = 75* with r the distance from the centre of the coordinate system to the receiver point. Figure 4-3 gives exactly the same results as Figure 5 of [Hussar], validating our propagation model in the case of a 2D dielectric cylinder.
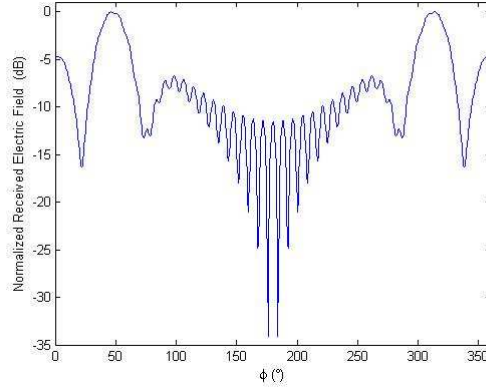

Figure 4-3: Results for the Figure 5 scenario of [Hussar]

4.2. 3D VALIDATION FOR A CONDUCTING CYLINDER USING A LITERATURE REPORT

This validation was made with the report of [Govaerts] who developed a 3D UTD solution for the scattering of obliquely incident electromagnetic waves by a perfectly conducting circular cylinder of arbitrary radius and finite length. But what was the most interesting is its experimental verification in 3D considering a spherical wave incidence and an isotropic antenna. The geometrical situation for the measurement is given on Figure 4-4.
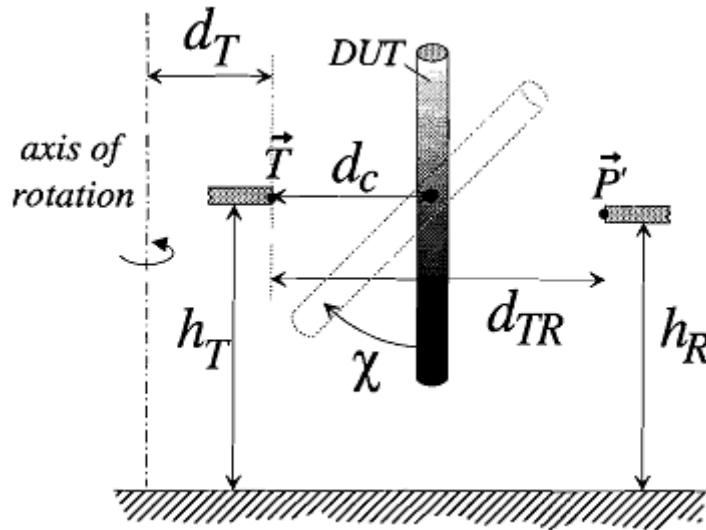

Figure 4-4: Parameters for the measurement setup of [Govaerts]

The cylinder is the *Device Under Test (DUT)* and has a length of approximately *70 cm*. $\vec{T}$ and $\vec{P'}$ correspond to the Transmitter and Receiver positions respectively. h_T = *1498 mm* is the height of the Transmitter and h_R = *1443 mm* is the height of the Receiver. d_T = *452 mm* and d_{TR} = *699 mm*. d_c corresponds to the horizontal distance measured between the cylinder axis of

symmetry and $\vec{T}$. Moreover, the cylinder can be rotated in the vertical plane containing $\vec{T}$ and $\vec{P}'$ by an angle χ. The measurements were performed for different normalized radius R/λ, for the 2 polarizations, over the frequency range $f \in [46, 54]$ GHz but the data were only stored for the centre frequency $f_c = 50$ GHz. Finally, the azimuth angle span of the observation point range was taken $\phi \in [-12°, 12°]$, with a step of 0.1°.

First, five cylinders of different radius (R/λ = 0.5-5) are used as a DUT, with χ = 0° (cylinder axis = z axis). The results obtained with our 3D propagation model are presented for the extreme values, i.e. R/λ = 0.5 and R/λ = 5 on Figures 4-5 and 4-6 respectively.
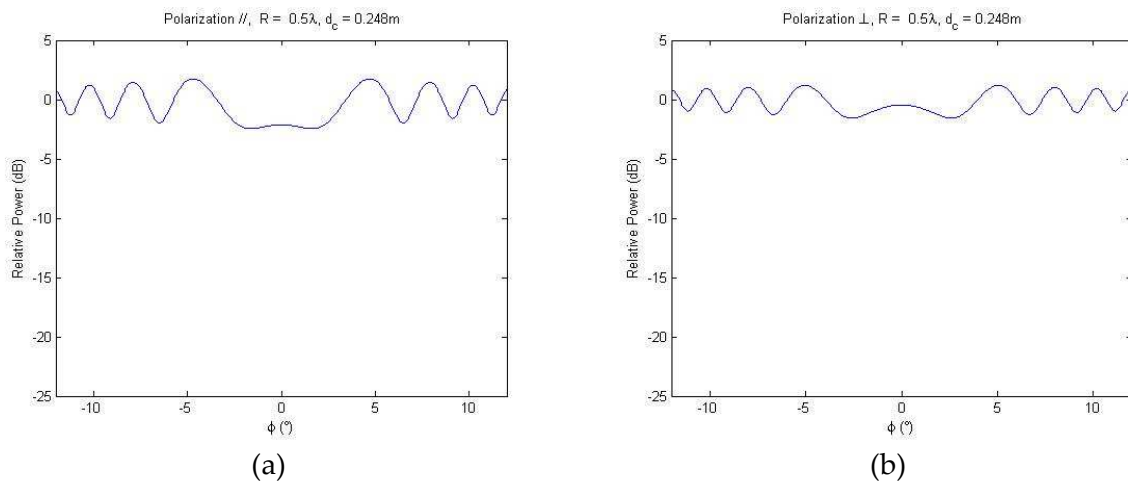

(a)   (b)

Figure 4-5: Results for R/λ = 0.5 for (a) polarization // and (b) polarization ⊥.

The obtained results on Figures 4-5(a), 4-5(b), 4-6(a) and 4-6(b) are exactly the same as the ones of Figures 5.10, 5.11, 5.18 and 5.19 of [Govaerts] respectively. We would have the same conclusion for results obtained for the other normalized radius not treated in this document. Moreover the Govaerts model results are very close to his measurements: we can say, at this stage, that our model is valid in 3D for a perfectly conducting cylinder.

Secondly, to verify the results for oblique incidence, the cylinder with radius R/λ = 1.5 was also mounted in a slanted position, with χ = 22.1° (±0.1°). The results obtained with our model are given on Figure 4-7 for the 2 polarizations.

They are, once again, exactly the same results as the simulations of Govaerts (cf. Figures 5.20 and 5.21 of [Govaerts]). But, this time, the agreement between the measurements and these simulations is less for this oblique incidence: this difference is explained in [Govaerts].
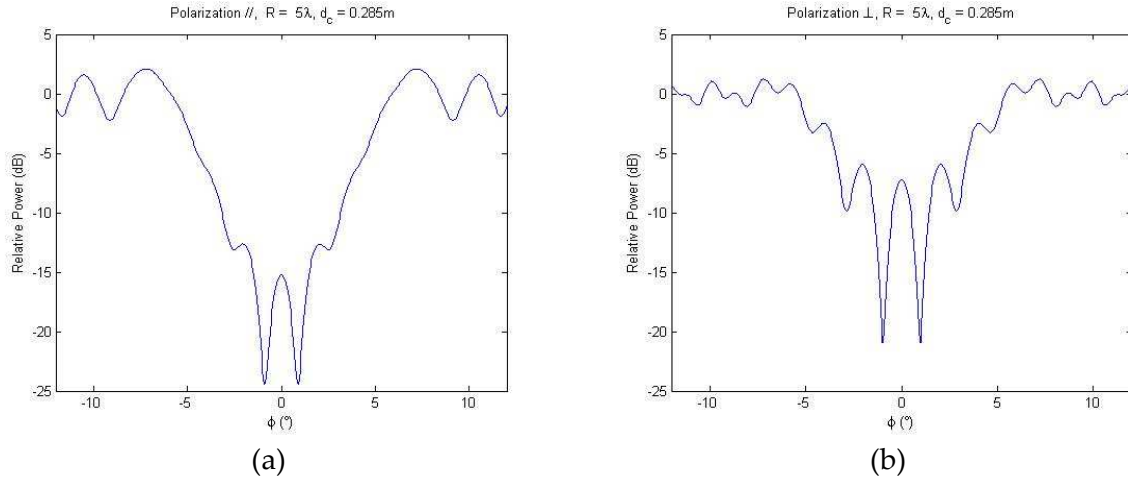
(a)   (b)

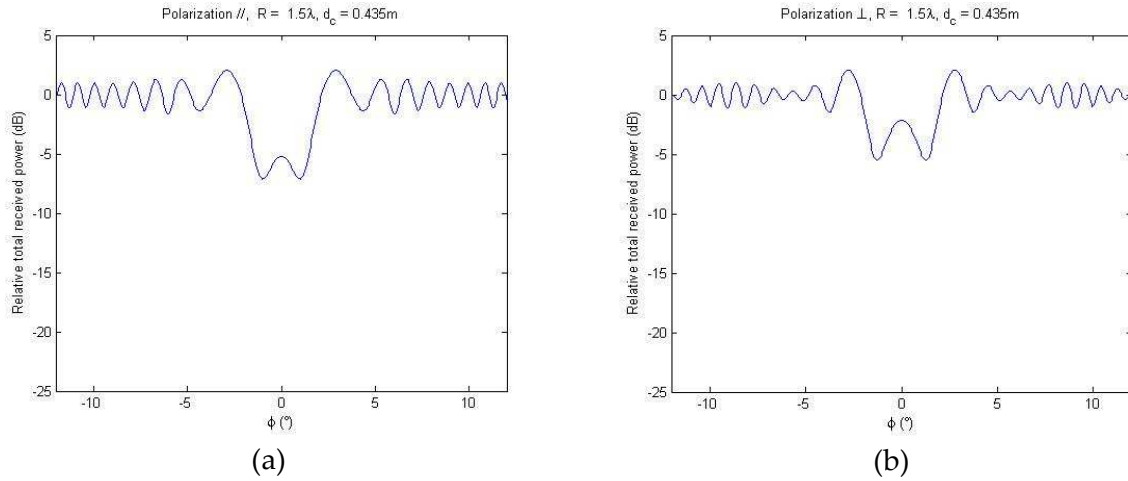**Figure 4-6: Results for R/λ = 5 for (a) polarization // and (b) polarization ⊥.**

(a)   (b)

Figure 4-7: Results for χ = 22.1° and R/λ = 1.5 for (a) polarization // and (b) polarization ⊥.

5. COMPARISON WITH UR1 SERIES S2 MEASUREMENT CAMPAIGN

Finally, we have compared the developed model described in this report with measurements made by UR1 team in the Satimo SG32 near-field antenna measurement chamber of IETR. The measurement campaign description is detailed in Part 2 of [Mhedhbi 1]. The chamber and the measurement platform (with an antenna and the considered cylinder called phantom) are described in details in [Mhedhbi 1]. Moreover, the Receiver Point is considered to be far from the cylinder.

5.1. PHANTOM CHARACTERISTICS

The custom built phantom was a nearly cylindrical plastic bottle filled with MLS1800 phantom liquid. The size of the phantom (height = 140 mm and R = 35 mm (cf. Figure 2-9 of [Mhedhbi 1])) was chosen to represent a human arm, while still being light enough for the platform to support it. The complex permittivity of the phantom liquid was given in [Mhedhbi 2] for the frequency range [300 MHz, 3 GHz] and summarized in Table 5-1. Interpolation of the dielectric characteristics of the phantom liquid is possible in frequency

range of Table 5-1 but the measurements were made in the [800 MHz, 5.95 GHz] frequency range. So we don't have access to the dielectric properties of the cylinder between 3 GHz and 5.95 GHz: we decided to use, for this frequency range, the dielectric properties given by [Koutitas] based on the "Muscle" model: $\varepsilon_r = \varepsilon_r^{'} = 48.2$ and $\sigma = 4.7\, S/m$, values used, in this article, for a frequency of 5 GHz.

f (GHz)	0.3	0.6	0.9	1.2	1.5	1.8	2.1	2.4	2.7	3
$\varepsilon_r^{'}$	58.15	57.03	55.99	54.94	53.64	52.63	51.67	50.40	49.28	47.82
$\varepsilon_r^{''}$	20.28	13.96	12.90	13.44	14.14	14.86	15.72	16.73	17.53	18.31
σ (S/m)	0.34	0.47	0.65	0.90	1.22	1.49	1.84	2.23	2.63	3.06

Table 5-1: Dielectric parameters of the phantom liquid
given in the [300 MHz, 3GHz] frequency range

5.2. UTD MODEL ADAPTATION

The only measurement series of [Mhedhbi 1] that is interesting for the present developed propagation model is the series S2: this series was done to measure how the antenna response varies in the presence of the phantom with various antenna-phantom distances (we will call "d" this antenna-phantom distance). The measurements were made for $0° \leq \phi < 360°$ and $0° < \theta < 180°$ with a step of approximately 2°. Antenna Th1 was used for all runs of Series S2. Data file 'S2R1' gives us the antenna response. Data files 'S2R2' to 'S2R23' gives us the measurement with phantom at different radial distances using the groove, from d= 30 mm (File 'S2R2') to d = 135 mm (File 'S2R23'), with a distance step of 5 mm.

Moreover, we could use the antenna response of 'S2R1' file in our model in order to take into account the real antenna used for measurements. Indeed, the antenna Th1 is not exactly isotropic in polarization θ (corresponding to the polarization ⊥ used before) and has less gain in polarization ϕ (corresponding to the polarization // used before) than in polarization θ. This last remark makes us finding the exact directions (ϕ_e, θ_e) of the emitted rays in direction of the considered interaction (reflection or attachment point). For the moment, only a comparison in 2D between our model results and the measurements is done so we have only θ = 90°. So we make a simple linear interpolation between 2 measurements points of S2R1 to find the exact value of antenna response in the direction of the considered ray. Therefore, the incident field at the interaction point P_I, which is at a distance s^I from Tx, will finally be expressed as:

$$E_{//,\perp}^{i}(P_I) = F(\phi_e, \theta_e) \cdot \frac{e^{-jks^I}}{s^I} \tag{24}$$

with the couple $(P_I, s^I) = (Q_R, s^i), (Q_1, s_1^i)\, or\, (Q_3, s_2^i)$ according to the studied ray, and $F(\phi_e, \theta_e)$ will be the antenna response in the direction (ϕ_e, θ_e) of the studied incident field.

5.3. 2D COMPARISON

Comparisons between UTD results and measurement are only given for a 2D configuration, i.e. in the azimuth plane (θ = 90° and 0°< ϕ< 360°) because we have to adapt the model (bilinear interpolation of the antenna response has not been performed for the moment) for a comparison in 3D. We decided to present in this report the comparisons made for 3 different distances *d* between the antenna and the cylinder: 3 cm, 9 cm and 13 cm. The results are given and analyzed below for these 3 different distances, for 3 frequencies:

- f=900 MHz : the lowest frequency for which we know the exact dielectric properties of the cylinder;

- f=3 GHz : the highest frequency for which we know the exact dielectric properties of the cylinder;

- f=5.95 GHz : the highest frequency for which we have measurements results and for which we use the cylinder dielectric properties of [Koutitas].

5.3.1 FOR A DISTANCE OF 3 CM

Figure 5-1 gives the obtained results for the UTD developed model and the measurements for 900 MHz. The comparison is not convincing for polarization θ (cf. Figure 5-1(a)), i.e. the maxima and the minima for the model and the measurements seems to be in "phase opposition". It is not the case in polarization ϕ (cf. Figure 5-1(b)), apart from the case of ϕ = 180° for which the model predicts a maximum and the measurements a minimum. For 900 MHz, the wavelength is λ = 33.33 cm which is large enough regarding the distance and the cylinder radius: we are maybe at the limit of UTD theory application, which explains that the results are not good for this first distance.
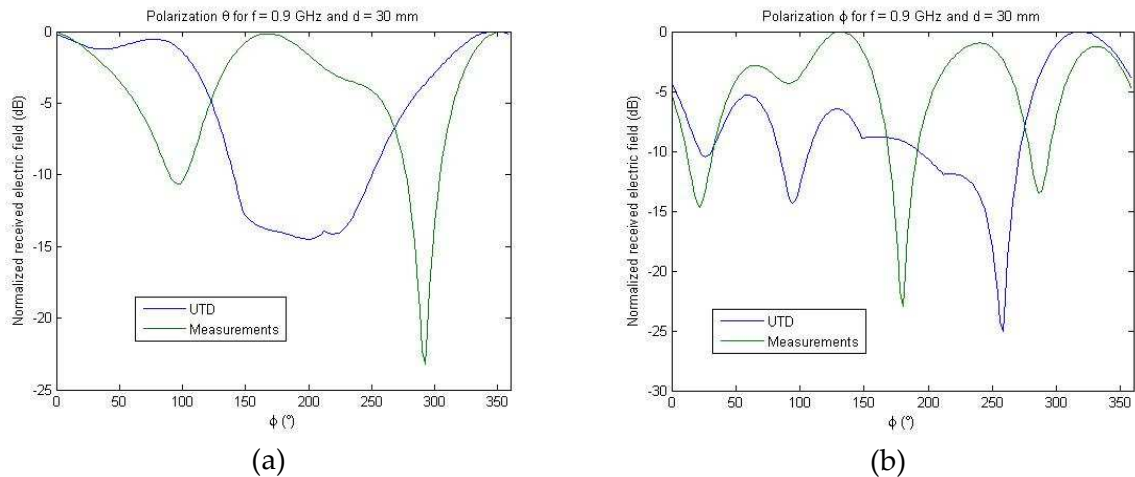

(a)   (b)

Figure 5-1: Comparison between UTD results and measurements for f = 900 MHz for (a) polarization θ and (b) polarization ϕ

On the other hand, for 3 GHz and 5.95 GHz (cf. Figures 5-2 and 5-3 respectively), results are very good in polarization θ (cf. Figures 5-2(a) and 5-3(a) respectively): the model predicts a maximum at ϕ = 180°, which was expected from the theory because the "creeping waves"

PROGRAMME
INFRASTRUCTURES MATERIELLES ET
LOGICIELLES POUR LA SOCIETE
NUMERIQUE – ED. 2011

ANR

CORMORAN

called rays 1 and 2 above, arrived in phase at the receiver in a 2D configuration. The measurements give also a maximum for this particular value of θ, weaker than for the model at 3 GHz but greater than for the model at 5.95 GHz. This predicted field in the shadow zone is the first improvement regarding the 3D additive model of [Mhedhbi 1] which doesn't predict anything in the shadow zone although, as it is highlighted by the UR1 measurements, a diffracted field exists and presents a maximum at ϕ = 180° for 2D configuration.

Concerning the polarization ϕ, comparison is quite good for 3 GHz (cf. Figure 5-2(b)): more oscillations are observed for the UTD results but the "shape" of the 2 curves are globally the same. But we notice a "phase opposition" in the case of 5.95 GHz (cf. Figure 5-3(b)): maybe other propagation phenomena have to be taken into account (diffractions by the top and the bottom of the cylinder could have more influence in the phase of the received field because the wavelength is weaker than the ones corresponding to 900 MHz and 3 GHz).
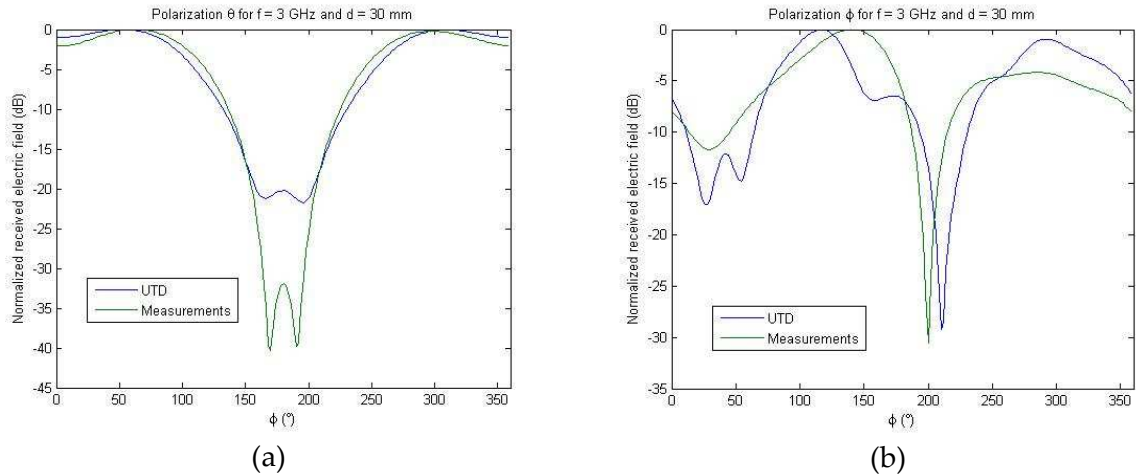

(a)   (b)

Figure 5-2: Comparison between UTD results and measurements for f = 3 GHz for (a) polarization θ and (b) polarization ϕ

(a)   (b)
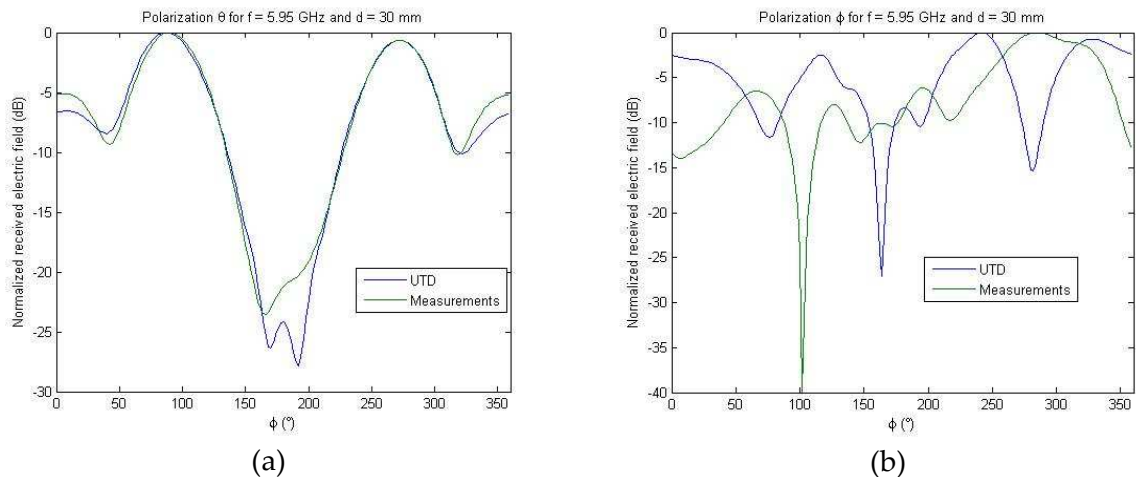
Figure 5-3: Comparison between UTD results and measurements for f = 5.95 GHz for (a) polarization θ and (b) polarization ϕ

5.3.2   FOR A DISTANCE OF 9 CM

Figure 5-4 gives the results for 900 MHz: the comparison between model and measurements, regarding the case of d = 3 cm studied previously, is quite good. The maximum at φ = 180°, for polarization θ in the shadow zone (cf. Figure 5-4(a)), is obtained for the measurements as well as for the UTD model: maybe it is due to the fact that, this time, the distance d is larger. Concerning polarization φ (cf. Figure 5-4(b)), results are quite good but with the same conclusion as for d = 3 cm: for φ = 180°, the model predicts a maximum and the measurements a minimum.

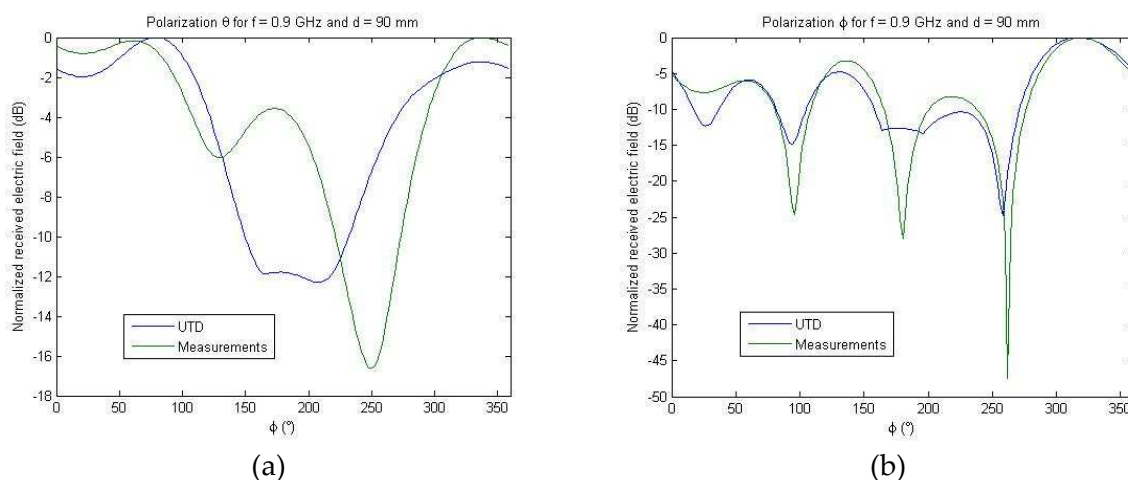

(a)   (b)

**Figure 5-4: Comparison between UTD results and measurements for f = 900MHz
for (a) polarization θ and (b) polarization φ**

Figures 5-5 and 5-6 give the comparison results for 3 GHz and 5.95 GHz respectively. We notice, for these 2 frequencies and polarization θ (cf. Figures 5-5(a) and 5-6(a) respectively for 3 GHz and 5.95 GHz), a very good correspondence between the model predicted results and the measurements, with the same conclusions as for the case of d = 3 cm.
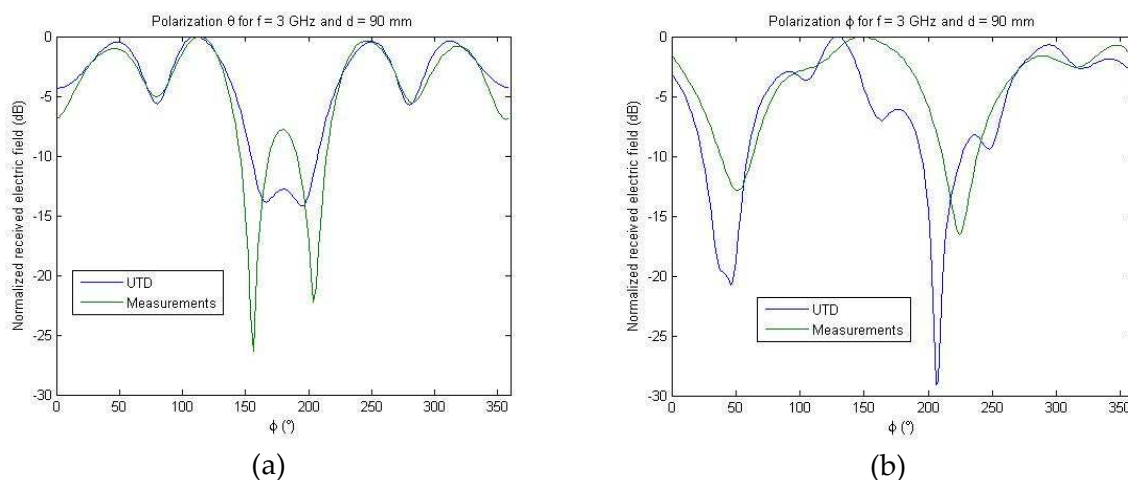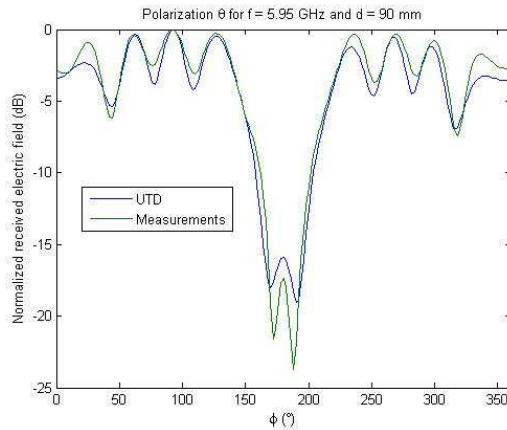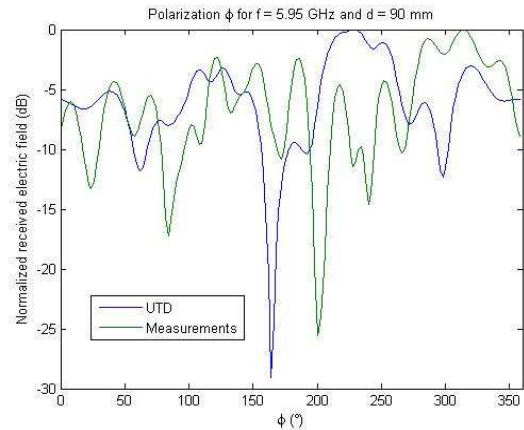

(a)   (b)

**Figure 5-5: Comparison between UTD results and measurements for f = 3 GHz
for (a) polarization θ and (b) polarization φ**

For polarization ϕ and 3 GHz (cf. Figure 5-5(b)), more oscillations are observed for the UTD results but the curves "shape", as it was already the case for 900 MHz, are nearly the same.

For polarization ϕ and 5.95 GHz (cf. Figure 5-6(b)), comparison is better than for d = 3 cm, with little more oscillations in the case of the measurements, maybe due to the diffracted fields at the top and bottom of the cylinder.


(a)   (b)

Figure 5-6: Comparison between UTD results and measurements for f = 5.95 GHz for (a) polarization θ and (b) polarization ϕ

5.3.3   FOR A DISTANCE OF 13 CM

Concerning this new distance, we can say that we have globally the same conclusions than for the distance d = 9 cm for the frequencies 900 MHz and 3 GHz, for which the comparisons are illustrated by Figures 5-7 and 5-8 respectively.
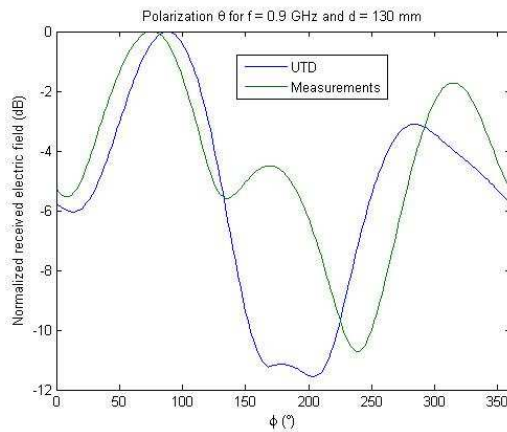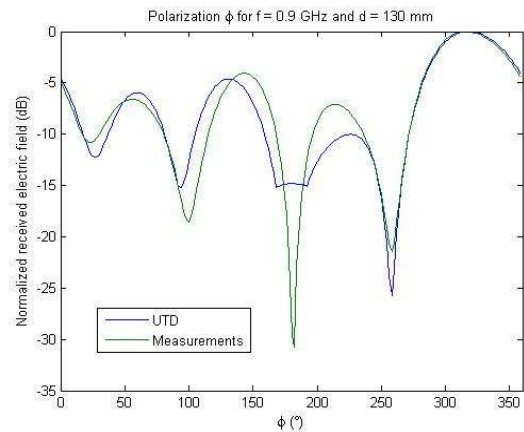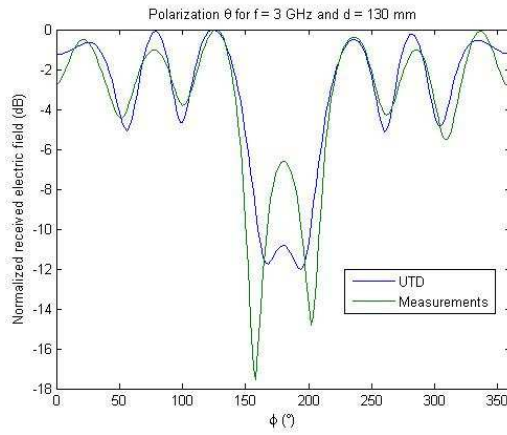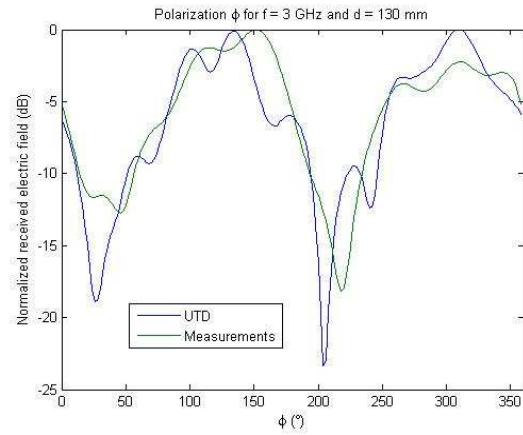

(a)   (b)

Figure 5-7: Comparison between UTD results and measurements for f = 900 MHz for (a) polarization θ and (b) polarization ϕ
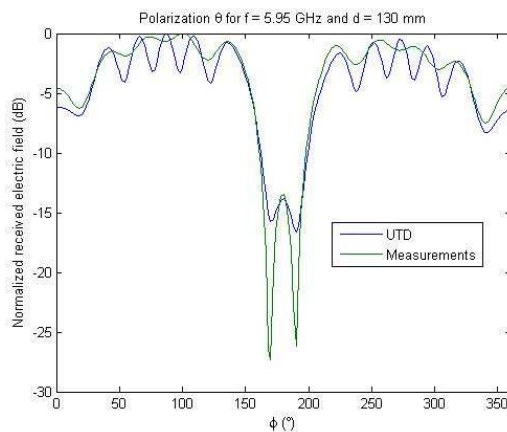
(a)   (b)

Figure 5-8: Comparison between UTD results and measurements for f = 3 GHz
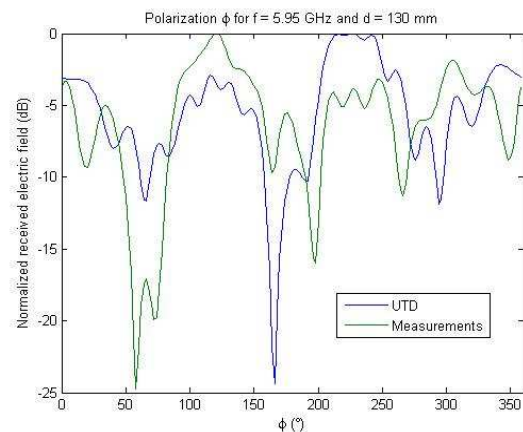**for (a) polarization θ and (b) polarization ϕ**

On the other hand, new conclusions appear for the comparison in the case of 5.95 GHz, as illustrated by Figure 5-9.

For polarization θ (cf. Figure 5-9(a)), the comparison between the model and the measurement results in the shadow region (168°< ϕ< 192°) is quite good. The problem appears in the lit region in which we notice 1 more oscillation in the case of the UTD model: but globally, the results "shapes" are quite the same.

For polarization ϕ (cf. Figure 5-9(b)), UTD model varies a little more rapidly than the measurements, which was the inverse case for 2 distances studied previously. But, globally, the obtained curves for the UTD model and the measurements have the same shape.

(a)   (b)

Figure 5-9: Comparison between UTD results and measurements for f = 5.95 GHz
for (a) polarization θ and (b) polarization ϕ

6. CONCLUSIONS

A 3D deterministic propagation model, based on the ray-tracing technique and the UTD, developed for the particular case of a 3D single dielectric cylinder of finite length, has been described and validated in 2D (for conducting and dielectric cylinders) and 3D (conducting cylinder). Moreover, the first 2D comparisons of the model with the UR1 measurements series S2 presented in [Mhedhbi 1] are quite encouraging. 3D comparisons with these same measurements will follow: for this, we have to modify the 3D UTD received electric field computed with our model (a bilinear interpolation has to be applied on the 3D antenna response in order to use the good value of antenna gain in the direction of the considered emitted ray). Moreover, if these new comparisons reveal a good correspondence between UTD model results and measurements, this new UTD model will be validated in 3D for a dielectric cylinder, which is not available in the literature for the moment (cf. Part 4 of this report).

Then, we could model 2 other possible scenarios concerning the transmitter and the receiver point positions towards the cylinder: the "Radiation" scenario (when the Transmitter (the Receiver) is on the cylinder and the Receiver (the Transmitter) is far from the cylinder) and the "Coupling" scenario (when both Transmitter and Receiver are on the cylinder). These scenarios imply the computation of new integrals, different from the *Pekeris* function expressed in equation (19). We can think also to develop the model for not only a circular cylinder but for the more general case of an elliptic cylinder.

Then we can study the possibility of adapting the present described model for the scenario of several cylinders in order to really model the human body. After, we can imagine a dynamic model taking into account the human body motion... Then we could imagine a scenario with several persons.

The originality of the model developed in this report is its deterministic nature and its ability to take into account the dielectric nature of the human body. Fast statistical models already exist but don't model the electromagnetic wave paths. Other techniques (as FDTD ("Finite Difference Time Domain")) model the propagation environment in a very detailed way but with a very long computation time. The UTD model is an intermediate model in terms of propagation environment description and computation time. If it could be optimized in term of computation time and, if it could be adapted for a complete human body (i.e. several cylinders), it maybe could be used as a future WBAN model...

7. REFERENCES

[Mhedhbi 1] M. Mhedhbi, Stéphane Avrillon, Bernard Uguen, Melsuine Pigeon, Raffaele D'Errico and Pierre Pasquero", D2.1 - On-Body Antennas Characterization & Exploitable Radiation Properties", Technical Report, CORMORAN (ANR 11-INFR-010) Project , 57 pages, October 31, 2012.

[McNamara] D.A. McNamara, C.W.I. Pistorius, J.A.G. Malherbe "Introduction to the Uniform Geometrical Theory of Diffraction", Artech House, Boston, 1990.

[Pathak] P.H. Pathak, W.D. Burnside and R.J. Marhefka, "A Uniform GTD Analysis of the Diffraction of Electromagnetic Waves by a Smooth Convex Surface", IEEE Trans. on Antennas and Propagation, Vol. AP-28, N°5, pp. 631-642, September 1980.

[Hussar] P.E. Hussar, "A Uniform GTD Treatment of Surface Diffraction by Impedance and Coated Cylinders", IEEE Trans. on Antennas and Propagation, Vol. 46, N°7, pp. 998-1008, July 1998.

[Govaerts] H.J.F.G. Govaerts, "Electromagnetic Wave Scattering by a Circular Cylinder of Arbitrary Radius", Report of Graduation Work, performed October 1992 – August 1993, 62 pages.

[Glaeser] G. Glaeser, "Reflections on Spheres and Cylinders of Revolution", Journal for Geometry and Graphics, Vol. 3, N°2, pp. 121-139, 1999.

[Kouyoumjian] R.G. Kouyoumjian and P.H. Pathak, "A Uniform Geometrical Theory of Diffraction for an Edge in Perfectly Conducting Surface", Proceedings of the IEEE, Vol. 62, N°11, pp. 1148-1461, November 1974.

[Plouhinec] E. Plouhinec, "Etude et Extension de Modèles de Prédiction de la Propagation. Elaboration d'un Serveur Expert Multi-Modèles", PhD Dissertation D 00-13, INSA de Rennes, Décembre 2000.

[Bouche] D. Bouche and F. Molinet, "Méthodes Asymptotiques en Electromagnétisme", Springer, 416 pages, 1994.

[Abramovitz] M. Abramovitz and I.A. Stegun, "Handbook of Mathematical Functions", Dover Publications Inc., New-York, 1965.

[Wait] J.R. Wait and A.M. Conda, "Diffraction of Electromagnetic Waves by Smooth Obstacles for Grazing Angles", Journal of Research of the National Bureau of Standards, Vol. 63D, N°2, pp. 181-197, September-October 1959.

[Pearson] L. Wilson Pearson, "A Scheme for Automatic Computation of Fock-Type Integrals", IEEE Trans. on Antennas and Propagation, Vol. 35, N° 10, pp. 1111-1118, October 1987.

[Medgyesi] L.N. Medgyesi-Mitschang, D-S. Wang, "Hybrid Solutions for Large-Impedance Coated Bodies of Revolution", IEEE Trans. on Antennas and Propagation, Vol. AP-34, N°11, pp. 1319-1328, November 1986.

[Mhedhbi 2] M. Mhedhbi, "Requirements for UWB Antenna Electromagnetic Simulations", CORMORAN Working Document, October 23, 2012.

[Koutitas] G. Koutitas, "Multiple Human Effects in Body Area Networks", IEEE Antennas and Wireless Propagation Letters, Vol. 9, pp. 938-941, 2010.